Structure and magnetic properties of nanocrystalline $Sm(Fe_{1-x}Co_x)_{11}Ti$ ($x \leqslant 2$)

L. Bessais and C. Djega-Mariadassou
LCMTR, UPR209, Centre National de la Recherche Scientifique, 2/8 rue Henri Dunant, Boite Postale 28, F-94320 Thiais, France
(Received 29 June 2000; published 4 January 2001)

Magnetic properties correlated to structural transformations, from metastable hexagonal $CaCu_5$-type phases to equilibrium tetragonal 1:12 phases, are studied systematically for nanocrystalline $Sm(Fe_{1-x}Co_x)_{11}Ti$ alloys ($x \leqslant 2$). The Rietveld analysis gives a stoichiometry ratio equal to 1:10, for the out of equilibrium hexagonal precursor, which is described with three crystallographic transition-metal T sites: $3g$ is fully occupied, and $6l$ occupation is limited to hexagons surrounding the T dumbbell pairs $2e$. The substitution of Co, in both structures, contributes to reduce the negative exchange interactions and results in Curie temperature enhancement. The hyperfine parameter assignment, on the basis of the Wigner-Seitz volume calculation, in the tetragonal structure points towards the Co $8f$ preferential occupation. The mean hyperfine field increase, with Co content, in the two phases, might be correlated to the compensation of the core-electron polarization field by the $4s$ polarization field produced by the $3d$ moment. The coercitive field of 0.6 T measured at room temperature suggests that nanocrystalline $SmFe_9Co_2Ti$, with a Curie temperature equal to 790 K, is a semihard material and is a potential candidate for magnetic recording.

DOI: 10.1103/PhysRevB.63.054412 PACS number(s): 75.50.Bb, 75.50.Tt, 76.80.+y

I. INTRODUCTION

The rare-earth iron intermetallic compounds are of interest from an application point of view and in understanding fundamental physics and metallurgical properties. The two main areas of application for magnetic materials are magnetic recording (semihard magnets) and dynamic and static permanent magnet applications (hard magnets).

After the discovery of the Nd-Fe-B permanent magnets,[1] research began for new Fe-based intermetallic phases that might be suitable as permanent magnets. So far, iron-rich and rare-earth-containing phases with the tetragonal $ThMn_{12}$ crystal structure have attracted the most attention.[2–4]

The ternary compounds $R(Fe,M)_{12}$ (R = rare earth, M = Ti,V,Mo, . . .) with the $ThMn_{12}$-type tetragonal structure are known to be possible candidates for permanent magnet materials.[2,4–6] When the R atom has a positive Stevens coefficient, the easy axis of the magnetization is along the crystallographic axis c. The effect of the third element M is considered to be essential for stability and magnetic properties of the alloys.[6] The occupation criteria relative to the stabilizing metal depend on steric effects and enthalpy values concerning the R-M bond.[7] Attractive features of the $RFe_{12-x}M_x$ compounds are their relatively simple tetragonal crystalline structure. So, these compounds are of interest for understanding fundamental physics problems.

The synthesis of a number of rare-earth–transition-metal alloys by mechanical alloying has recently been reported.[8,9] Optimally, heat-treated structures have been shown to exhibit high coercive forces and isotropic behavior associated with nanocrystalline microstructures, indicating that mechanical alloying is a very interesting preparation method to achieve the permanent magnet application of rare-earth–transition-metal alloys.

In a continuing program of study relative to structural and magnetic properties of rare-earth iron intermetallic compounds, we have investigated $ThMn_{12}$ structure compounds. This is because with this structure, on the basis of the composition, which is rich in $3d$ metals, a high saturation magnetization would be expected, and, due to the large ratio of a/c, a strong magnetocrystalline anisotropy is hopeful.

In order to understand more fully the phase formation of the mechanically alloyed (MA) Sm-Fe-Co-Ti powders, we carried out a systematic investigation of the effects of the cobalt substitution and the annealing conditions on the structure and the magnetic properties of a tetragonal $SmFe_{11}Ti$ semihard nanocrystalline alloy. It is well known that preparation techniques such as mechanical alloying, high-frequency sputtering, or melt-spinning produce disordered phases and precursors to the known equilibrium phases.

A detailed description of the relationship between the disordered hexagonal precursor and the ordered 1:12 structure will be first presented. Afterwards, structure results relative to the known stoichiometric 1:12 phase will be used to explain the hexagonal parent, with information about diffraction domain size, lattice stress, and nature of minor phases. Curie temperature evolution will attest for the pertinence of the Fe substitution in both phases. The Co site preference in the 1:12 phase will be demonstrated by Mössbauer spectroscopy and will provide the interpretation of the disordered phase Mössbauer spectra. The effect of nanocrystallinity on coercivity will be finally reported. The study of the $SmFe_{11-x}Co_xTi$ series has been limited up to $x=2$, where the easy direction of magnetization of the tetragonal phase remains axial.[10]

II. EXPERIMENT

Intermetallic compounds $SmFe_{11-x}Co_xTi$ with Co concentration $x=0$, 0.5, 1, 1.5, and 2 were prepared from elemental powders of 99.9% pure Sm, Fe, Ti, and Co with respective particle size 40, 325, 50, and 50 mesh, milled in a high-energy Fritsch P7 planetary ball mill to form an ultrafine layered microstructure. Mixtures of the powders were sealed in a hardened steel vial together with five 15 mm diameter steel balls. A ball to powder mass ratio of 15:1 was

used with milling time of 5 h. A high-purity, argon-filled glove box with an O_2 and H_2O rate around 1 ppm was used for loading and sealing the vials and all post-milling powder handling. The as-milled powder was wrapped in tantalum foil and sealed in silica tubes under a vacuum of 5×10^{-7} Torr, then annealed for 30 min at temperatures between 923 and 1423 K.

The overall chemical composition of all samples was checked by inductively coupled plasma atomic emission spectroscopy (ICP-AES) and appeared, within the experimental uncertainties (± 0.04), in agreement with the nominal composition. Energy-dispersed x-ray spectrometry (EDX) with LINK AN10000 equipment and a beam size of 25 nm, mounted on a JEM 100 CX II microscope, was employed to analyze specifically the $ThMn_{12}$-type structure of all alloys annealed at 1423 K.

The crystal structure was deduced from x-ray-diffraction (XRD) patterns, registered on a Brucker diffractometer with automatic divergence slit (Cu $K\alpha$ radiation $\lambda = 1.541\,78$ Å). The x-ray spectra were refined using the FULLPROF program based on the Rietveld method.[16,17]

The peak-shape function was chosen as Thompson-Cox-Hastings pseudo-Voigt type.[18] As a measure of the quality of refinement, two agreement factors (R_B and χ^2 will be defined in Sec. IV A) from the program output were used.

The magnetization was measured using a Manics differential sample magnetometer (DSM) in magnetic fields up to 1.8 T. When necessary, the samples were sealed in silica tubes to avoid oxidation upon heating.

Thermomagnetic data were measured under an applied field of 1000 Oe with a heating rate of 10 K/min. The Curie temperature T_C was determined from the M-T curves by extrapolating the linear part of the M-T curve and finding the temperature values of the intersection with the extended baseline.

^{57}Fe Mössbauer spectra were obtained between 77 and 300 K, with a 50 mC ^{57}Co/Rh source, on a constant-acceleration 512-channel spectrometer. The calibration, performed with α-iron foil, gave a linewidth for the external peaks of 25 mm/s. The sample's natural iron concentration was around 12 mg/cm^2. The parabolic distortion of the spectra was canceled by working in the mirror image mode, and the small resulting linear drift of the baseline was corrected. The spectra were fitted as discussed in Sec. IV and the estimated errors were at most ± 0.1 T for hyperfine fields, ± 0.005 mm/s for isomer shifts, and ± 0.01 mm/s for the quadrupole shifts.

III. STRUCTURAL CONSIDERATION OF THE AB_5 PHASE AND DERIVED STRUCTURES

The stoichiometric RT_5 structure of $CaCu_5$ $P6/mmm$ type can evolve to nonstoichiometric $P6/mmm$ structures. Atomic ordering generates phases with discrete composition 2:17, 3:29, and 1:12 indicative of $R\bar{3}m$, $P2_1/C$, and $I4/mmm$ space groups. The homogeneity range of the hexagonal phase varies with R and T elements. For R=Y and T=Co, an upper limit of Co content, 7.3, has been reported.[11] The R-Fe precursors are generally described as having $TbCu_7$ structure except the $P6/mmm$ $SmFe_9$ phase, which we reported[12] as the parent phase of Sm_2Fe_{17} in agreement with Teresiak *et al.*[13] It is worth noting that the $P6/mmm$ precursor to the 1:12 $I4/mmm$ structure of the $Sm(Fe,Co)_{12}Ti$ alloys was considered up to now as a $TbCu_7$ phase. Preliminary considerations about the structure relationship are required to justify the model used in the structure refinement.

The lattice parameters of the tetragonal $ThMn_{12}$-type phase can be converted into those of hexagonal $CaCu_5$-type phase according to the following conversion equations:

$$a_{1:5} = c_{1:12} \quad \text{and} \quad c_{1:5} = \frac{a_{1:12}}{2}.$$

Furthermore, when two dumbbell pairs (T-T) substitute for $2R$ atoms over a $4RT_5$-type cell, the $ThMn_{12}$-type phase occurs as follows:

$$4(RT_5) - 2R + 4T(\text{dumbbell}) \rightarrow 2(RT_{12}).$$

RT_5 is constituted by the R lattice built at the coordinate origin $1a$ (0,0,0) and $2T$ sublattices built on $2c$ ($\frac{1}{3},\frac{2}{3},0$) and $3g$ ($\frac{1}{2},0,\frac{1}{2}$) positions. This arrangement leads to two types of layers: in the lowest one, R atoms are centered on T hexagons, whereas in the next layer only T atoms are accommodated.

The T-excess region of the RT_5 unit cell has been described by the formula $R_{1-s}T_{5+2s}$, where s expresses the number of R substitutions. In the low-excess T region ($s \simeq 0.12$) Givord *et al.*[14] have proposed the following scheme for Sm-Co alloys: if $(1-s)$ is the R occupation rate in the (0,0,0) $1a$ position, with decreasing R content, $2sT$ atom pairs substitute the R positions. They constitute the dumbbell pairs located on the $(0,0,Z)$ $2e$ position. The initial $2c$ hexagons shift towards the c axis in the position $6l$ [$(X,2X,0)$; $X < \frac{1}{3}$]. As a consequence, only $2(1-3s)T$ atoms remain located in the special $2c$ position ($\frac{1}{3},\frac{2}{3},0$) and four T crystallographic sites are necessary to explain the T-excess $P6/mmm$ structure. Nevertheless, the $P6/mmmRT$ precursor of the ordered $R\bar{3}m$ 2:17 structure and the $I4/mmm$ structure known as $TbCu_7$-type phase have not been described with the $6l$ site.[15]

From $s=0$ up to $s=0.33$, the $6l$ population increases while the $2c$ decreases from 2 down to 0, with a theoretical equipartition for $s=0.16$ (see Table I). Moreover, high enrichment gives evidence of the additional $6l$ site by the fact that only the $2c$ site cannot describe such T content.

In this paper, we intended to extrapolate the Givord *et al.*'s model towards higher s values ($s \geqslant 0.33$). This model gives the possibility to take into account the T distortion obviously brought by the R substitution. The more general $6l$ site, which involves the previous $2c$ hexagons, implies an atom occupation rate limited to $\frac{1}{3}$. At most one-third of $6l$ T atoms forming hexagons surround the dumbbell $2e$ (Fig. 1). We have applied such theoretical substitution mechanisms to the hexagonal precursor of the $ThMn_{12}Sm(Fe,Co)_{12}Ti$ with three iron sites $2e$, $6l$, and $3g$ (see Table I).

TABLE I. Atom Wyckoff positions, number of subsequent atom in the parent $R_{1-s}T_{5+2s}$ hexagonal $P6/mmm$ structure as a function of the s parameter atom occupancy, and Wyckoff positions with numbers of subsequent atoms in the RT_{12} $I4/mmm$ tetragonal structure.

Atom position	$R_{1-s}T_{5+2s}$				Atom position	RT_{12}
	$s=0$	$0<s<0.33$	$s=0.33$	$s>0.33$		
Sm $(1a)$ 0,0,0	1	1-s	0.66	1-s	Sm $(2a)$ 0,0,0	2
T_1 $(2c)$ $\frac{1}{3},\frac{2}{3},0$	2	2(1-3s)	0	0	T_1 $(8f)$ $\frac{1}{4},\frac{1}{4},\frac{1}{4}$	8
T_2 $(6l)$ X,2X,0		6s	2	2	T_2 $(8i)$ X,0,0	8
T_3 $(2e)$ 0,0,Z		2s	0.66	2s	T_3 $(8j)$ $X,\frac{1}{2},0$	8
T_4 $(3g)$ $\frac{1}{2},0,\frac{1}{2}$	3	3	3	3		

We used the known atom distribution of the well-established $ThMn_{12}$-type structure to deduce atomic population in the $P6/mmm$ structure. No drastic atom modification over change was expected. Most particularly Ti and Co distribution in the hexagonal precursor ought to be close to those of the descent.

The tetragonal RT_{12} phase is characterized by three crystallographic nonequivalent T sites: $8i$, $8j$, $8f$. One-half of the atoms on the $6l(2c)$ site in the $P6/mmm$ RT_5 motif become equivalent to the pair of substitution atoms and form the $8i$ site. One-third of the atoms on the $3g$ site and the remaining half of the atoms in the $6l$ $(2c)$ site of the $P6/mmm$ cell constitute the $8j$ site. The other two-thirds of the $3g$ site constitute the $8f$ site.

Although XRD is not sensitive to the Co and Fe distribution, we will adopt such a relationship to fit the $P6/mmm$ structure. Keeping in mind that the Ti atom site results from an evolution of $P6/mmm$ $2e$ and $6l$ population, and $8f$ atoms provide the $3g$ site. These observations will constitute the basis of the model used for the analysis of XRD diagrams and Mössbauer spectra relative to the hexagonal $P6/mmm$ RT_5-type phase.

However the binary RT_{12} structure does not exist and needs to be stabilized by a third element that occupies the $8i$ site.[19] Ti is one of the stabilizing elements of the binary Fe-Sm alloy. In the case of the $YFe_{11-x}Co_xTi$ compounds, Co atoms are known to occupy preferentially the f site in bulk material.[20] Fe atoms are located on the j site and the remaining fraction on the i and f sites.

The distribution of Co in the $Sm(Fe,Co)_{11}Ti$ alloys still remains a problem open to discussion. As a matter of fact, XRD cannot distinguish the Co and Fe positions due to their close atomic diffraction factor. A neutron diffraction study is difficult to carry out owing to the samarium absorption. Mössbauer spectroscopy appears to be a powerful technique to define the preferential occupation of Co in 1:12 structure; we will discuss this point in Sec. IV B.

IV. RESULTS AND DISCUSSION

A. Structural properties

The x-ray diagrams of the as milled samples reveal the lines of a bcc α-Fe–Ti and Co solid solution. At low angles, a background increase that results from the collapse of the samarium lines is associated with amorphous samarium as corroborated by Mössbauer spectroscopy. An additional solid-state diffusion reaction at low annealing temperature

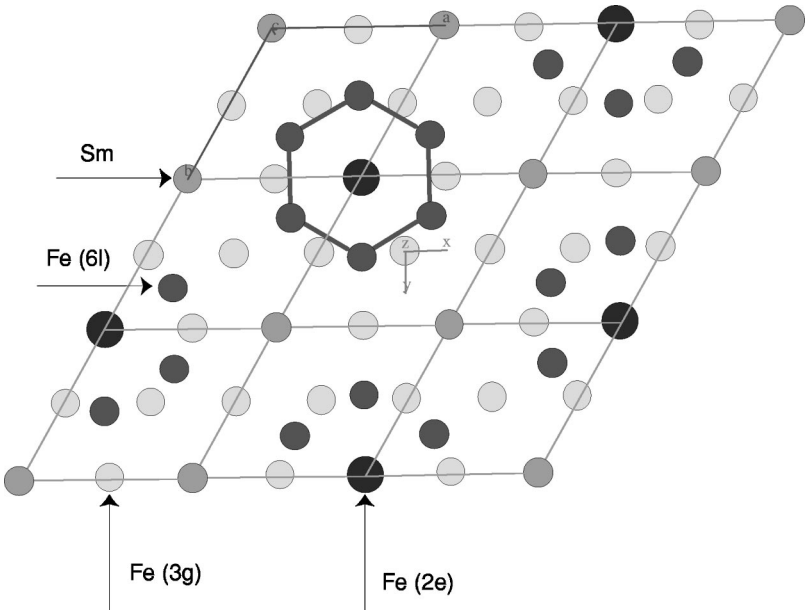

FIG. 1. Two-dimensional (001) projection of the partially disordered hexagonal $P6/mmm$ structure. $6l$ hexagons surround the dumbbell iron site $2e$.

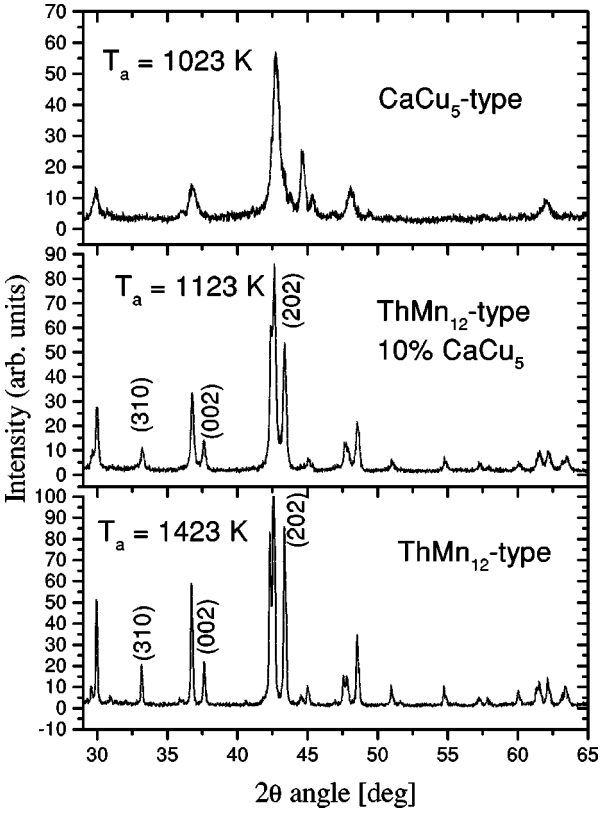

FIG. 2. X-ray diagram of $SmFe_{10.5}Co_{0.5}Ti$ annealed at 1023, 1123, and 1423 K.

T_A leads for all x content to the hexagonal $P6/mmm$ structure. The ordered phase of $ThMn_{12}$ type $I4/mmm$ is obtained above 1023 K.

As an example, the XRD spectra of three MA samples with the composition $SmFe_{10.5}Co_{0.5}Ti$ annealed at 1423 K, 1123 K, and 1023 K respectively, are shown in Fig. 2. At 1023 K, the XRD diagram can be indexed according to the hexagonal $P6/mmm$ structure. With increasing annealing temperature, $1073 < T_A < 1173$ K, a more ordered state appears, indicated by the gradual emergence of superstructure reflection peaks denoted by *hkl* (202), (002), (202), indicative of the $ThMn_{12}$ type structure $I4/mmm$. Moreover, the broadening of the diffraction peaks reduces at high annealing temperature. For $T_A = 1423$ K, the XRD pattern can be indexed unambiguously into the $ThMn_{12}$-type structure.

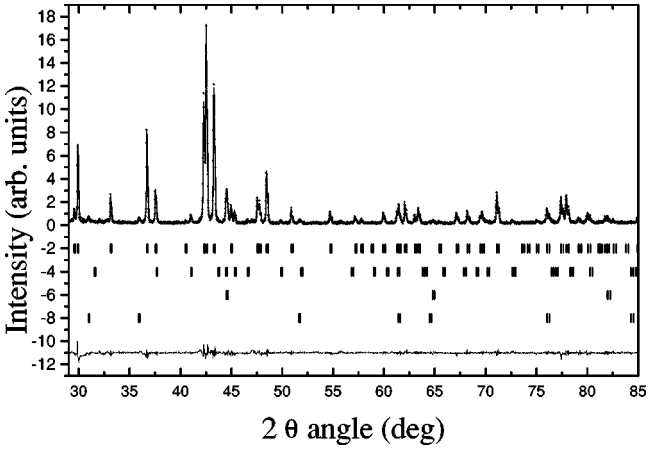

FIG. 3. Rietveld analysis for $SmFe_{11}Ti$ annealed at 1423 K. The set of ticks refer, respectively, to $SmFe_{11}Ti$, Fe_2Ti, α-Fe–Ti, and SmO-N.

The XRD diagrams of the annealed material at a temperature up to 1073 K show a main phase contribution of about 95 vol% for $0 < x < 2$, indexed by the disordered $CaCu_5$-type hexagonal $P6/mmm$ cell, in agreement with results from rapidly quenched[19] $SmFe_{11}Ti$. The additional weak lines are assigned to bcc α-Fe–T, around 2%; Fe_2Ti, 1%; and SmO-N, 2%.

In the Rietveld refinement process, the following various structure parameters were adjusted: atom positions, atom site occupancy, Debye-Waller factors, and cell parameters, together with the parameters describing the line profile. However, the structural model must be known *a priori* with parameters close to the real parameters.

The line broadening reflects microstrains and isotropic size effects. In order to evaluate those contributions, we have chosen a peak function of Thompson-Cox-Hastings pseudo-Voigt type, defined as a convolution of Lorentzian and Gaussian functions.

TABLE II. T composition of the $I4/mmm$ phase as given by EDX analysis for the various nominal composition x, a, and c cell parameters, D mean diffraction domain size, η strain rate, and R_B and χ^2 factors from the Rietveld fit for $T_A = 1423$ K.

	$x=0$	$x=0.5$	$x=1$	$x=1.5$	$x=2$
	Fe=10.97	Fe=10.46	Fe=9.96	Fe=9.45	Fe=8.96
T atoms	Ti=1.02	Ti=1.02	Ti=1.03	Ti=1.04	Ti=1.03
EDX analysis	Co=0	Co=0.5	Co=1.01	Co=1.51	Co=2.02
a (nm)	0.8555(3)	0.8552(3)	0.8555(3)	0.8552(3)	0.8555(3)
c (nm)	0.4794(3)	0.4791(3)	0.4788(3)	0.4787(3)	0.4785(3)
D (nm)	95	107	89	80	87
η (%)	0.18	0.26	0.33	0.30	0.36
R_B	3.79	5.21	4.94	5.61	6.47
χ^2	2.21	1.80	1.69	1.57	1.33
$X\{8i\}$	0.357	0.358	0.359	0.359	0.359
$X\{8j\}$	0.276	0.275	0.274	0.274	0.275

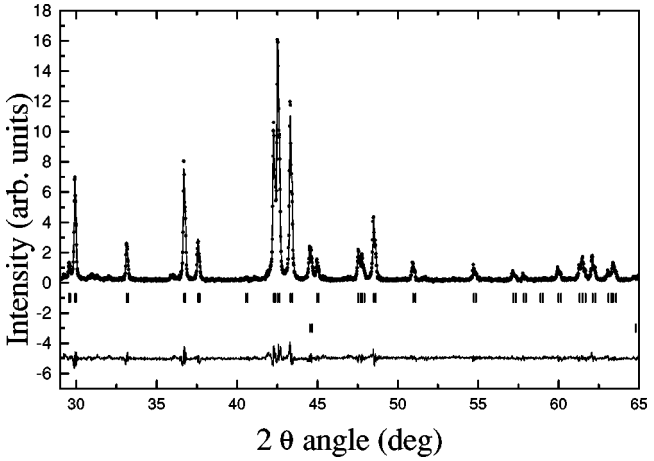

FIG. 4. Rietveld analysis for $SmFe_{10.5}Co_{0.5}Ti$ annealed at 1423 K. The set of ticks refer, respectively, to the main phase and α-Fe–(Ti,Co).

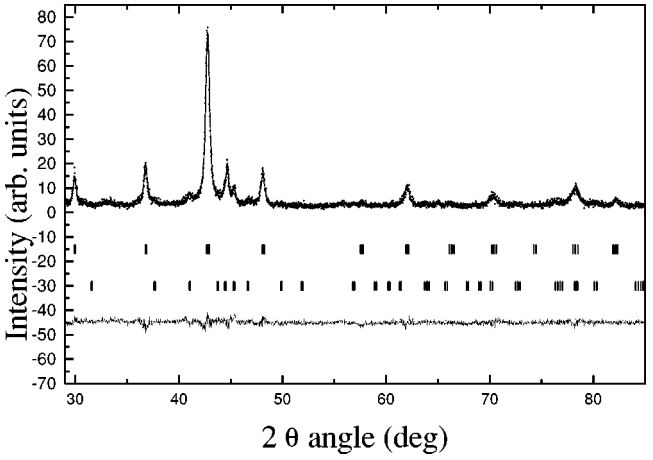

FIG. 5. Rietveld analysis for $SmFe_{10.5}Co_{0.5}Ti$ annealed at 1023 K. The set of ticks refer, respectively, to the hexagonal phase and SmO-N.

Isotropic Lorentzian and Gaussian contributions of size and microstrains were taken into account. The full width at half maximum of the Gaussian H_G and Lorentzian H_L component of the profile function is given by

$$H_G^2 = u \tan^2 \theta + v \tan \theta + w,$$

$$H_L = x \tan \theta + \frac{y}{\cos \theta},$$

where y provides a size value representing the volume-averaged diameter of crystallites in all directions. The u parameter leads to an estimate of the isotropic broadening due to strain effects.

The various structural parameters, X and Z atomic position, Debye-Waller factor, occupancy parameter s, cell parameter, and the u, x, and y profile parameters, are least-square fitted. The goodness-of-fit indicators are calculated as follows:

TABLE III. $P6/mmm$ characteristics deduced from the Rietveld fit; s is the atom occupancy parameter.

	$x=0$	$x=0.5$	$x=1.5$
s	0.439	0.422	0.404
Sm content	8.7	9.0	9.3
a (nm)	0.4899(3)	0.4899(3)	0.4906(3)
c (nm)	0.4225(3)	0.4232(3)	0.4232(3)
D (nm)	17	16	16
Strain rate (%)	0.45	1.00	1.00
R_B	3.84	6.21	5.57
χ^2	1.47	1.18	1.42
X	0.287	0.288	0.288
Z	0.295	0.299	0.295

$$R_B = \frac{\sum_K |I_K(o) - I_K(c)|}{\sum_K I_K(o)},$$

where $I_K(o)$ is the observed Bragg intensity and $I_K(c)$ is the calculated one, and

$$\chi^2 = \frac{\sum_i w_i |y_i(o) - y_i(c)|^2}{N - P + C},$$

where $y_i(o)$ is the intensity observed at the ith step in the step scanned powder diffraction pattern, $y_i(c)$ is that calculated, and w_i is the weight of the observation. N is the total number of points used in the refinement. P the number of refined parameters, and C the number of strict constraint function.

For samples annealed at 1423 K, the agreement between theoretical and experimental XRD diagrams related to the $ThMn_{12}$ phase was calculated with the Fe/Ti and Fe/Co ratio

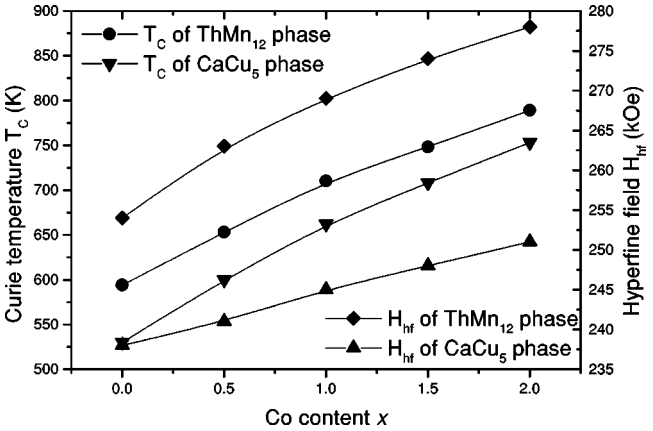

FIG. 6. Curie temperature and mean hyperfine field versus Co content x for $ThMn_{12}$ and $CaCu_5$ phases.

TABLE IV. Curie temperature T_C and the coercive field H_C for $SmFe_{11-x}Co_xTi$ annealed at 923 K, 1123 K, and 1423 K.

	H_C(T)			T_C(K)		
Co content x	$T_A=923$ K	$T_A=1123$ K	$T_A=1423$ K	$T_A=923$ K	$T_A=1123$ K	$T_A=1423$ K
0	0.07	0.41	0.20	526	594	595
0.5	0.08	0.55	0.20	599	652	653
1	0.07	0.56	0.18	664	710	710
1.5	0.07	0.57	0.190	728	747	748
2	0.07	0.60	0.19	748	789	789

given by the EDX analysis (see Table II). First, the refinement was performed with Ti and Co statistically distributed among all sites. Such hypothesis could be assumed owing to the preparation process of the material, which was out of equilibrium and possibly responsible for the high defect rate. However, the agreement was improved with Ti atoms distributed on i sites as observed for bulk material. The Co atoms were assumed to occupy the f site in analogy to $Y(FeCoTi)_{12}$.[20] Figures 3 and 4 show such a Rietveld refinement for samples with $x=0$ and $x=0.5$, respectively, as an example. The results concerning the fit of the various samples are given in Table II. It appears that the a parameter remains constant and equal to 0.8555 ± 0.0003 nm with increasing x. A noticeable decrease is observed for c from 0.4794 down to 0.4785 nm. The small trend to a reduction of the diffraction domain size together with an increase of the strain rate as the Co content increases might be consistent with the disorder brought by the fourth element slowing down the diffusion process. The higher size values remain still in the nanoscale range.

The Rietveld refinement of the hexagonal phase is more complex than that for the tetragonal case, for which the crystallographic atom occupancy parameter s is always equal to 1. The difficulties are linked to the fact that it grows at a lower temperature and the crystalline quality is not as good as that for the 1:12 phase. It results in a higher line broadening induced by higher strain rates and a smaller autocoherent diffraction domain size. Moreover, R and T sites, except $3g$, are atom deficient. Yet the model that we have adopted includes one unique occupancy parameter that correlates only two families, R and $2e$ T dumbbells. We have maintained the $6l$ occupancy rates equal to 0.33 to ensure the best geometrical equilibrium among T hexagons. In the fitting procedure, the parameter considered as free were the following: a, c, strain rate, diffraction domain size, R and T Debye-Waller factors, x and z Wyckoff parameters of $6l$ and $2e$ sites, and s occupancy parameter. The Ti and Co positions were deduced from the structure relationship between $I4/mmm$ and $P6/mmm$ phases with Ti and Co in i and f sites, respectively.

The results of the Rietveld analysis for the hexagonal $CaCu_5$ type phase are given in Table III for sample $x=0$, 0.5, 1.5, and an example of a Rietveld fit for sample $SmFe_{10.5}TiCo_{0.5}$ annealed at 1023 K is reported in Fig. 5.

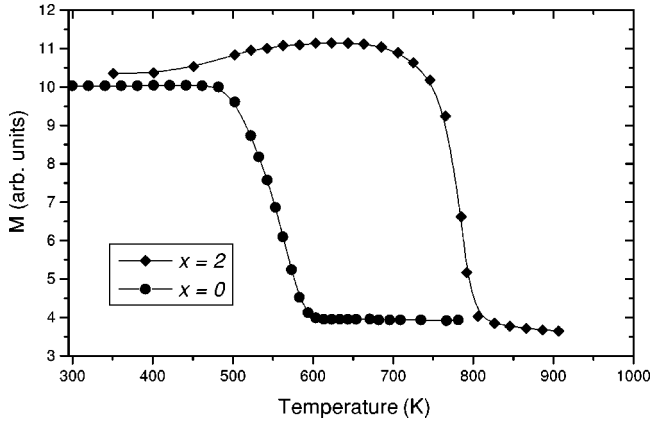

FIG. 7. Temperature dependence of the magnetization for $Sm(Fe_{1-x}Co_x)_{11}Ti$ compounds with $ThMn_{12}$ type structure for $x=0$ and $x=2$.

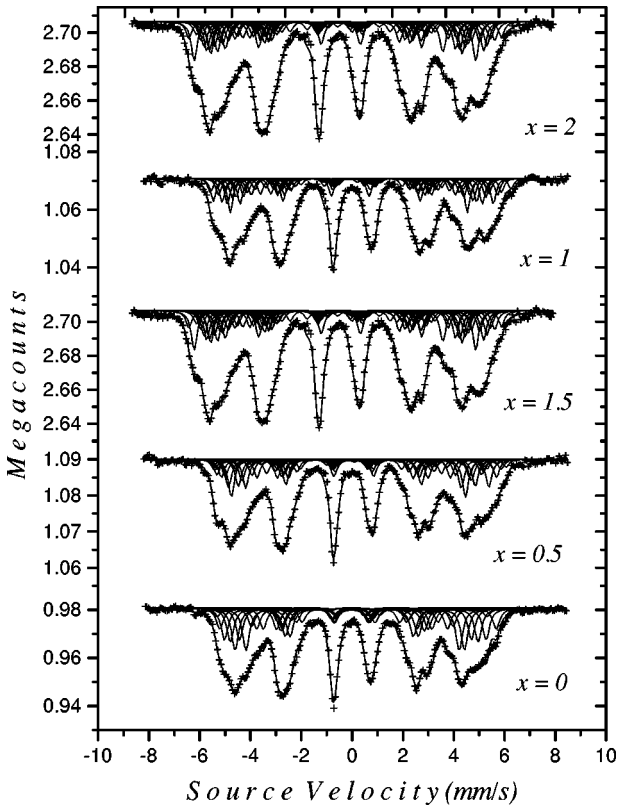

FIG. 8. The 77 K Mössbauer spectra of tetragonal $Sm(Fe_{1-x}Co_x)_{11}Ti$.

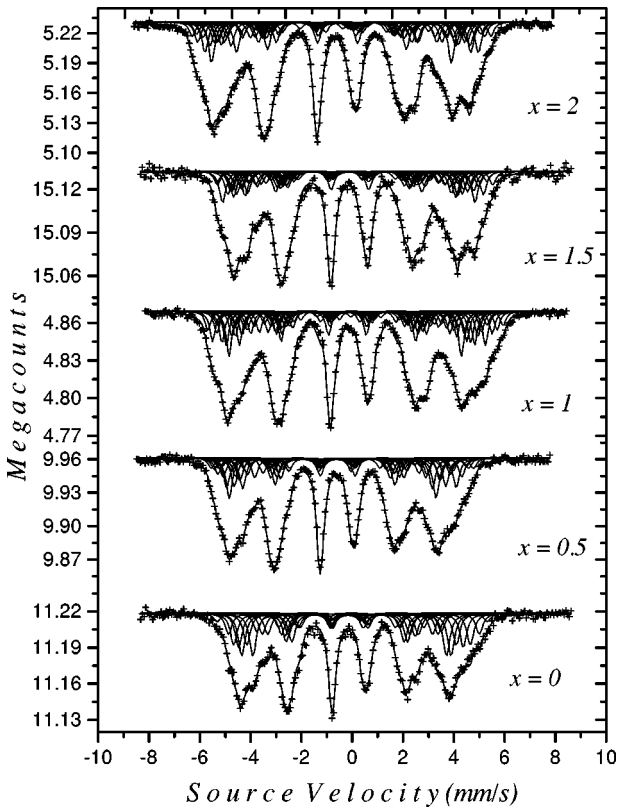

FIG. 9. The 300 K Mössbauer spectra of tetragonal $Sm(Fe_{1-x}Co_x)_{11}Ti$.

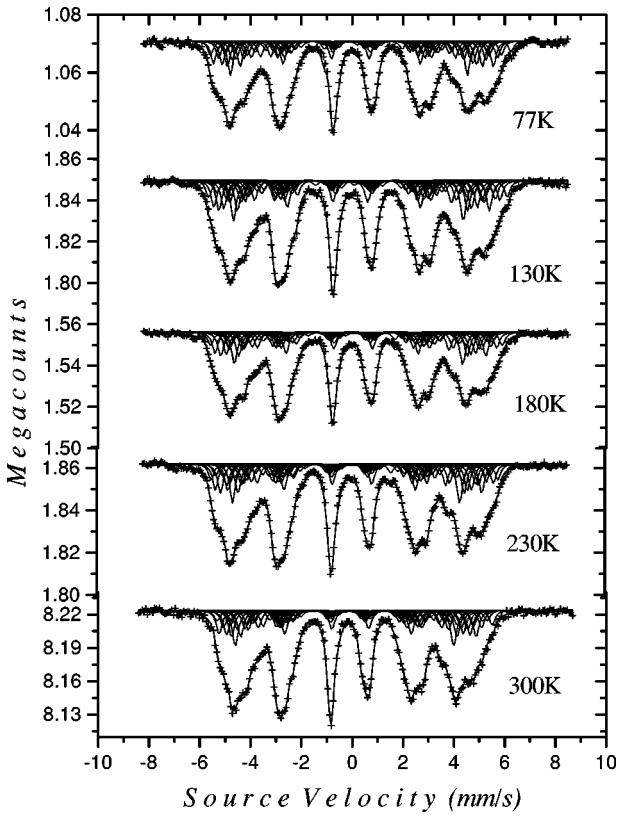

FIG. 10. The Mössbauer spectra of tetragonal $SmFe_{9.5}Co_{1.5}Ti$ obtained at the indicated temperatures.

The deduced samarium and transition-metal stoichiometry of the hexagonal phase is 1:10. The diffraction domain size is drastically reduced at 1023 K, reaching a lower range of nanocrystalline scale.

The higher amount of bcc iron compared with the higher-temperature diagrams might be due, first, to the fact that the diffusion process is slower at 1023 K and nonreacted iron is present with samarium poorly crystallized. Second, the hexagonal phase stoichiometry does not match exactly that of the 1:12 phase. We suggest that stoichiometry between both phases is recovered by stacking faults.

B. Magnetic properties

The Curie temperature T_C of the 1:12 compounds varies similar to the $R_2Fe_{14}B$ and R_2Fe_{17} systems. The Curie temperature is mainly determined by Fe-Fe exchange interaction. The compounds $R(Fe,Ti)_{12}$ show higher Curie temperature than the corresponding R_2Fe_{17} compounds. It is known that the Fe-Fe exchange interaction depends markedly on the interatomic distance.

The composition dependencies of the Curie temperatures T_C for the $SmFe_{11-x}Co_xTi$ alloys derived from thermomagnetic analysis results are shown in Fig. 6 and summarized in Table IV. With increasing Co content, the Curie temperature of the $ThMn_{12}$-type phase increases from 595 K ($x=0$) to 789 K ($x=2$) (see Table IV, Fig. 7).

The Curie temperature of the $CaCu_5$-type phase changes from 526 K for $x=0$ to 748 K for $x=2$. This indicates that the addition of the Co atom enhances the exchange interaction of the nearest-neighbor atoms in the Sm-Fe-Ti-Co series.

From Fig. 6 it can be seen that the Curie temperatures increase monotonically with increasing Co content for both structures ($ThMn_{12}$ and $CaCu_5$). There are three types of exchange interaction existing in $RFe_{11-x}M_x$ compounds, namely the R-R interaction between the magnetic moments on the R sublattice, the T-T interaction between the magnetic moments on the T sublattice, and the R-T intersublattice interaction. Among them, the T-T interaction is the strongest and determines the ordering temperature. It is well known

TABLE V. Wigner-Seitz derived near-neighbor environments and volumes in $SmFe_{11}Ti$.

Site	Sm{2*a*}	Fe{8*i*}	Fe{8*j*}	Fe{8*f*}	Iron near neighbors	WSC volume (Å^3)
Sm{2*a*}	0	4	8	8	18	30.56
Fe{8*i*}	1	5	4	4	11.75	18.84
Fe{8*j*}	2	4	2	4	9	11.94
Fe{8*f*}	2	4	4	2	9	11.64

TABLE VI. Mössbauer hyperfine parameter for $SmFe_{11}Ti$ ($x=0$, at $T=300$ K). Hyperfine field, H_{HF}; isomer shift, δ (relative to α-Fe at room temperature); relative area, S; and quadrupole splitting, ε.

Parameter	$8i_0$	$8i_1$	$8i_2$	$\langle 8i\rangle$	$8j_0$	$8j_1$	$8j_2$	$\langle 8j\rangle$	$8f_0$	$8f_1$	$8f_2$	$\langle 8f\rangle$
H_{HF} (T)	30.66	27.46	22.55	27.15	25.61	23.68	20.13	23.54	28.92	25.59	21.49	25.79
δ (mm/s)	0.02	−0.096	−0.092	−0.063	−0.048	−0.148	−0.101	−0.113	−0.061	−0.188	−0.116	−0.129
ε (mm/s)	0.052	0.015	0.063		0.047	0.032	0.045		0.043	−0.008	0.027	
S(%)	8	13	7		12	16	8		12	16	8	

that the T-T interaction is very sensitive to the distance between the transition-metal moments. Hu *et al.*[21] have reported that Fe at the $8i$ site has the largest magnetic moment while Fe at the $8f$ site has the smallest moment. The interatomic distances between the near neighbors of Fe atoms at the different sites are different. According to Givord and Lemaire,[22] there are two T-T exchange interactions in R_2Fe_{17} compounds, positive and negative. When the distance of the Fe-Fe pairs is smaller than 2.45 Å, the exchange interaction is negative, whereas at larger Fe-Fe distances the interaction is positive. It may be assumed that this is also the case in 1:12 systems. So, when the substitution of Co for Fe occurs at sites where the distance between Fe-Fe pairs is smaller than a certain critical distance, the negative interaction will be reduced and the total interaction will be enhanced, so that the Curie temperature will increase due to the substitution of Co for Fe.

Moreover, qualitatively, when the $3d$ band is nearly full, it is established that positive interactions dominate. For half-full band, competition exists between negative and positive interactions. The substitution of Co, which contributes to complete the $3d$ subband, reduces the negative interactions and induces the Curie temperature enhancement in both structures.

The $ThMn_{12}$-type phase Mössbauer spectra were measured between 77 and 300 K. The 77 and 300 K spectra, together with the fits, are presented in Fig. 8 and Fig. 9. At 300 K it is obvious that the mean hyperfine field increases with x (cobalt content) in agreement with Curie temperature variations. The same trend is observed at 77 K. The spectra for $x=1.5$, as an example, between 77 and 300 K, are shown in Fig. 10.

The analysis was performed according to the local environment of each of three crystallographic iron sites, taking into account the effect of titanium and cobalt near neighbors. Our model is based upon the two following assumptions: Ti and Co atoms occupy, respectively, $8i$ and $8f$ sites according to previous Mössbauer spectroscopy results on $YFe_{11}Ti$ and $Y(Fe,Co)_{11}Ti$ (Refs. 23 and 20) and neutron diffraction measurements on $Nd(FeTiCo)_{12}$ (Ref. 24).

For each individual sextet, Lorentzian linewidths of 0.27 to 0.29 mm/s were used. The area ratio of the absorption lines was assumed to be 3:2:1:1:2:3 because the absorber was a powder with randomly oriented particles, as corroborated by x-ray analysis.

From the Wigner-Seitz cell (WSC) calculation, we determined the near-neighbor environment and volumes. Iron near neighbors for the different sites $2a$, $8f$, $8i$, $8j$, and the WSC volumes were, respectively, 18, 9, 11.75, 9 and 30.56, 11.64, 18.84, 11.94 Å^3 (see Table V). During the analysis procedure, in the first step, we calculated the relative sextet areas by a binomial distribution law and fixed them. The average isomer shifts were classified on the basis of the WSC volumes, i.e., $8i>8j>8f$. In the last step, all hyperfine parameters were considered as free. The detailed approach was performed as follows.

For $x=0$, three sextets ought to be used at least to reproduce the spectra according to the existence of the three crystallographic i, j, f sites. However, more sextets are necessary to fit the spectra broadening. The statistical distribution of Ti atoms in site i influences the neighboring of each i, j, f Fe atom. The presence of 0, 1, 2 adjacent Ti neighbors to the i, j, f Fe atom was taken into account. Nine sextets were then used to simulate the experimental spectra i_0, i_1, i_2; j_0, j_1, j_2; f_0, f_1, f_2 (see Table VI).

In addition, each $8i$ iron has the most adjacent Fe atoms, 11.75 (see Table V), whereas each $8j$ and $8f$ Fe has only nine adjacent Fe neighbors. Thus, the largest hyperfine field should be attributed to the $8i$ site. However, it is difficult to assign properly the subspectra to the $8j$ and $8f$ site because the numbers of the site occupancies and the adjacent Fe atoms are the same for both sites. According to the neutron diffraction results[25] the local magnetic moment of the $8j$ site is larger than that of the $8f$. One can be tempted to correlate this result to the local hyperfine field. However, Coehoorn *et al.*[26] have shown that the contribution of the $4s$ electrons to the hyperfine field resulted in a significant deviation from a simple proportionality relation between the hyperfine field and the local Fe moments.

The correlation between WSC volume and isomer shift was demonstrated.[27,28] Moreover, the calculated sextet abundance for j_0 f_0, j_1 f_1, j_2 f_2 is, respectively, 12, 16, 8. The assignment of the various sextets to the different subsites was then carried out on the basis of the correlation between WSC volumes and δ.

The same approach was used for the Co compounds. The effect of 0, 1, 2, 3, 4 Co neighbors (for $x=2$) were considered, but to obtain a physically meaningful fit the relative abundance lower than 3% was neglected. The same model has been applied to all samples for each temperature.

The results of the above analysis are summarized in Table VII for $x=1$, as an example, the monotonic variation of the mean individual i, j, f site δ values as a function of temperature attests for the pertinence of the analysis (Fig. 11).

The isomer shift of the $8i$ and $8j$ atom shows a noticeable increase with Co substitution, while the $8f$-atom isomer shift remains quasiconstant [Fig. 12(a), Fig. 12(b)]. This result

TABLE VII. Mössbauer hyperfine parameter for $SmFe_{10}CoTi$ ($x=1$). Hyperfine field, H_{HF}; isomer shift, δ (relative to the α-Fe at room temperature); relative area, S; and quadrupole splitting, ε.

T(K)	Parameter	$8i_{00}$	$8i_{01}$	$8i_{10}$	$8i_{11}$	$8i_{20}$	$8i_{21}$	$\langle 8i \rangle$
300	H_{HF}	30.75	31.97	26.44	29.77	24.62	25.62	28.22
	δ	0.064	0.134	−0.054	−0.17	−0.269	0.359	−0.004
	ε	0.135	0.235	0.094	0.025	−0.044	0.278	
	S	3.3	4.4	5.6	7.4	3.7	4.9	
		$8j_{00}$	$8j_{01}$	$8j_{10}$	$8j_{11}$	$8j_{20}$	$8j_{21}$	$\langle 8j \rangle$
	H_{HF}	25.63	28.15	24.5	26.48	20.02	22.82	25.10
	δ	−0.074	−0.067	−0.191	−0.211	−0.085	−0.227	−0.095
	ε	0.075	0.089	0.046	0.09	0.074	−0.018	
	S	4.5	5.9	5.9	7.9	3.0	3.9	
		$8f_{00}$	$8f_{01}$	$8f_{10}$	$8f_{11}$	$8f_{20}$	$8f_{21}$	$\langle 8f \rangle$
	H_{HF}	29.88	31.53	26.72	29.86	22.46	24.0	27.47
	δ	0.02	−0.02	−0.228	−0.263	−0.153	0.048	−0.129
	ε	0.053	0.041	−0.068	−0.161	0.07	−0.025	
	S	7.9	3.0	10.6	7.1	5.3	3.5	
230		$8i_{00}$	$8i_{01}$	$8i_{10}$	$8i_{11}$	$8i_{20}$	$8i_{21}$	$\langle 8i \rangle$
	H_{HF}	26.33	35.02	28.29	29.38	28.48	28.57	29.42
	δ	0.064	0.199	0.193	−0.123	−0.732	0.464	0.027
	ε	0.76	−0.046	0.17	−0.013	0.331	0.268	
	S	3.3	4.4	5.6	7.4	3.7	4.9	
		$8j_{00}$	$8j_{01}$	$8j_{10}$	$8j_{11}$	$8j_{20}$	$8j_{21}$	$\langle 8j \rangle$
	H_{HF}	26.44	30.36	24.96	27.54	20.4	24.42	26.34
	δ	0.043	0.114	−0.063	−0.096	−0.058	−0.365	−0.061
	ε	0.123	0.02	−0.213	0.121	−0.03	−0.248	
	S	4.5	5.9	5.9	7.9	3.0	3.9	
		$8f_{00}$	$8f_{01}$	$8f_{10}$	$8f_{11}$	$8f_{20}$	$8f_{21}$	$\langle 8f \rangle$
	H_{HF}	31.89	32.36	27.73	31.23	23.29	25.07	28.73
	δ	−0.025	0.213	−0.223	−0.209	0.0123	−0.049	−0.103
	ε	0.024	0.179	−0.064	−0.073	0.014	0.078	
	S	7.9	3.0	10.6	7.1	5.3	3.5	
180		$8i_{00}$	$8i_{01}$	$8i_{10}$	$8i_{11}$	$8i_{20}$	$8i_{21}$	$\langle 8i \rangle$
	H_{HF}	25.56	35.68	28.69	29.85	28.77	29.11	29.75
	δ	0.558	0.138	0.168	−0.118	−0.71	0.492	0.059
	ε	0.796	0.024	0.21	−0.014	0.315	0.271	
	S	3.3	4.4	5.6	7.4	3.7	4.9	
		$8j_{00}$	$8j_{01}$	$8j_{10}$	$8j_{11}$	$8j_{20}$	$8j_{21}$	$\langle 8j \rangle$
	H_{HF}	26.92	30.88	25.25	27.94	21.48	24.75	26.81
	δ	0.008	0.099	−0.046	−0.067	−0.034	−0.335	−0.044
	ε	0.139	0.038	−0.205	0.109	0.009	−0.303	
	S	4.5	5.9	5.9	7.9	3.0	3.9	
		$8f_{00}$	$8f_{01}$	$8f_{10}$	$8f_{11}$	$8f_{20}$	$8f_{21}$	$\langle 8f \rangle$
	H_{HF}	32.39	32.61	27.9	31.84	23.84	25.33	29.12
	δ	−0.037	−0.12	−0.064	−0.208	−0.011	−0.049	−0.082
	ε	0.01	0.175	−0.073	−0.059	0.119	0.074	
	S	7.9	3.0	10.6	7.1	5.3	3.5	
130		$8i_{00}$	$8i_{01}$	$8i_{10}$	$8i_{11}$	$8i_{20}$	$8i_{21}$	$\langle 8i \rangle$
	H_{HF}	28.05	34.0	28.96	30.0	29.0	30.7	29.89
	δ	0.328	0.25	0.154	−0.082	−0.361	0.351	0.100
	ε	0.697	−0.015	0.304	−0.093	0.314	0.326	
	S	3.3	4.4	5.6	7.4	3.7	4.9	

TABLE VII. (*Continued*).

T(K)	Parameter	$8j_{00}$	$8j_{01}$	$8j_{10}$	$8j_{11}$	$8j_{20}$	$8j_{21}$	$\langle 8j\rangle$
	H_{HF}	26.75	31.05	25.72	28.13	22.5	25.18	27.01
	δ	0.052	0.184	0.008	−0.009	−0.12	−0.323	−0.015
	ε	0.163	0.009	−0.234	0.032	0.027	−0.408	
	S	4.5	5.9	5.9	7.9	3.0	3.9	
		$8f_{00}$	$8f_{01}$	$8f_{10}$	$8f_{11}$	$8f_{20}$	$8f_{21}$	$\langle 8f\rangle$
	H_{HF}	33.05	33.37	28.08	32.21	24.68	25.52	29.27
	δ	−0.02	−0.025	−0.046	−0.125	−0.15	−0.025	−0.054
	ε	0.027	0.158	−0.106	−0.128	0.103	0.105	
	S	7.92	2.57	10.60	7.07	5.25	3.53	
77		$8i_{00}$	$8i_{01}$	$8i_{10}$	$8i_{11}$	$8i_{20}$	$8i_{21}$	$\langle 8i\rangle$
	H_{HF}	33.71	35.56	27.72	31.1	25.56	27.74	30.15
	δ	0.448	0.178	0.107	−0.212	0.232	0.345	0.132
	ε	0.36	−0.031	0.09	0.107	0.05	0.549	
	S	3.3	4.4	5.6	7.4	3.7	4.9	
		$8j_{00}$	$8j_{01}$	$8j_{10}$	$8j_{11}$	$8j_{20}$	$8j_{21}$	$\langle 8j\rangle$
	H_{HF}	25.95	31.0	27.74	29.64	22.75	25.05	27.76
	δ	−0.02	0.02	−0.046	−0.1	0.179	−0.015	0.040
	ε	0.08	0.08	−0.139	0.132	0.077	−0.13	
	S	4.5	5.9	5.9	7.9	3.0	3.9	
		$8f_{00}$	$8f_{01}$	$8f_{10}$	$8f_{11}$	$8f_{20}$	$8f_{21}$	$\langle 8f\rangle$
	H_{HF}	32.53	34.1	28.98	31.73	24.98	25.56	29.13
	δ	0.21	−0.13	−0.072	−0.142	−0.009	−0.185	−0.007
	ε	0.112	0.066	−0.058	−0.204	0.056	0.05	
	S	7.9	3.0	10.6	7.1	5.3	3.5	

can be understood in terms of the preferential Co atom occupation. The $8i$ and $8j$ site Fe atoms have four adjacent $8f$ neighbors and the $8f$ site atoms have only two. The isomer shift behavior of the $8i$ and $8j$ site Fe atom is attributed to the additional $3d$ electrons brought by $8f$ Co neighbors. They enhance the shielding of the $4s$ electrons, reduce the s charge density at the nucleus, and result in an increasing isomer shift. In contrast, if $8f$-atom surrounding is poorly affected by the Co substitution, the s charge density is then not modified. No change is observed for the $8f$ isomer shift. The difference for the $8f$-site behavior then corroborates the preferential occupation of Co atoms on this site. Meanwhile, the dependence with composition of the average isomer shift can be considered as linear within a good approximation.

The nuclear hyperfine field H_{HF} variation corroborates too the validity of the field assignment reported as a function of temperature for $x=1$ (Fig. 13) and versus Co content x [Fig. 14(a), Fig. 14(b)] at 300 and 77 K. One must remember that $H_{HF}\{8f\}$ is larger than $H_{HF}\{8j\}$, unlike the $8f$ and $8i$ local magnetic moments measured by neutron diffraction. The reason is that neutron measurement involves the core part of the atom. The main contribution to the hyperfine

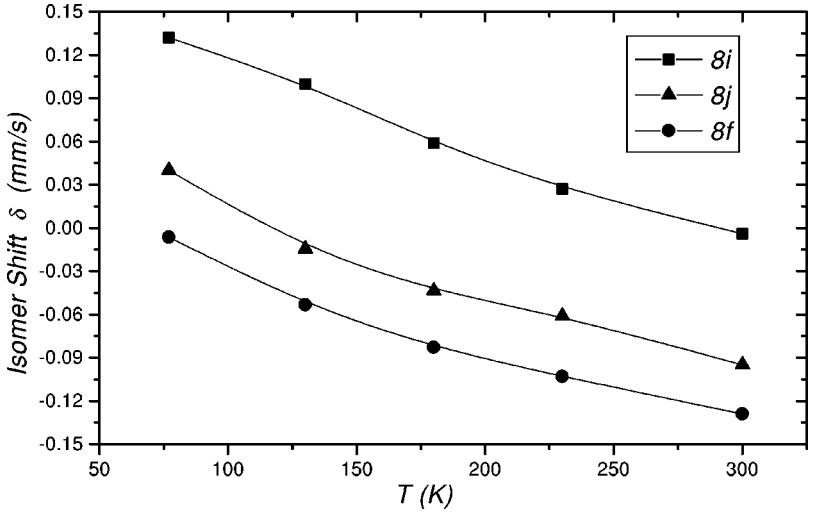

FIG. 11. The temperature dependence of the isomer shifts in $SmFe_{10}CoTi$.

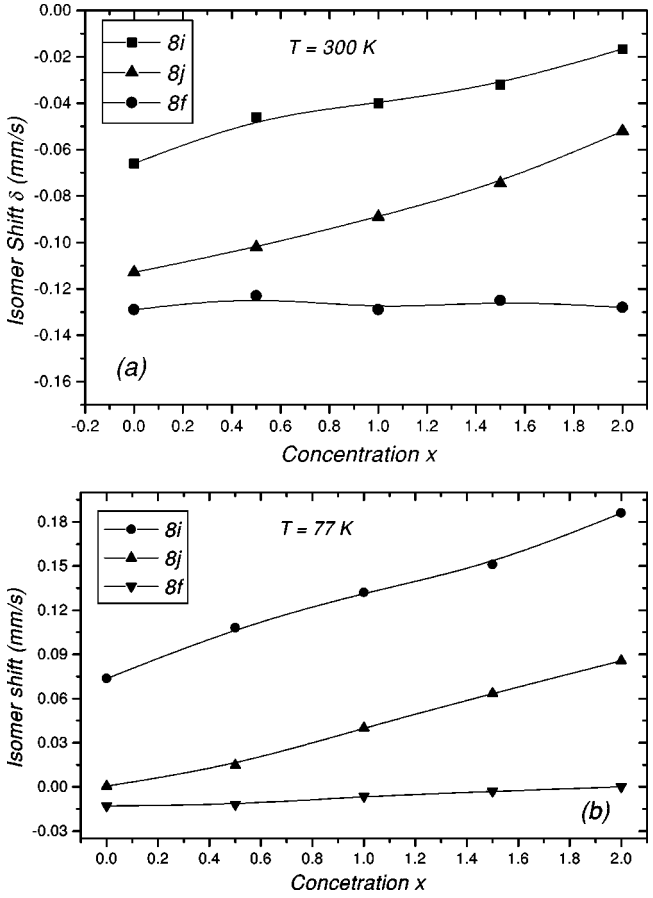

FIG. 12. The compositional dependence of the isomer shifts for the tetragonal 1:12 phase (a) at 300 K, (b) at 77 K.

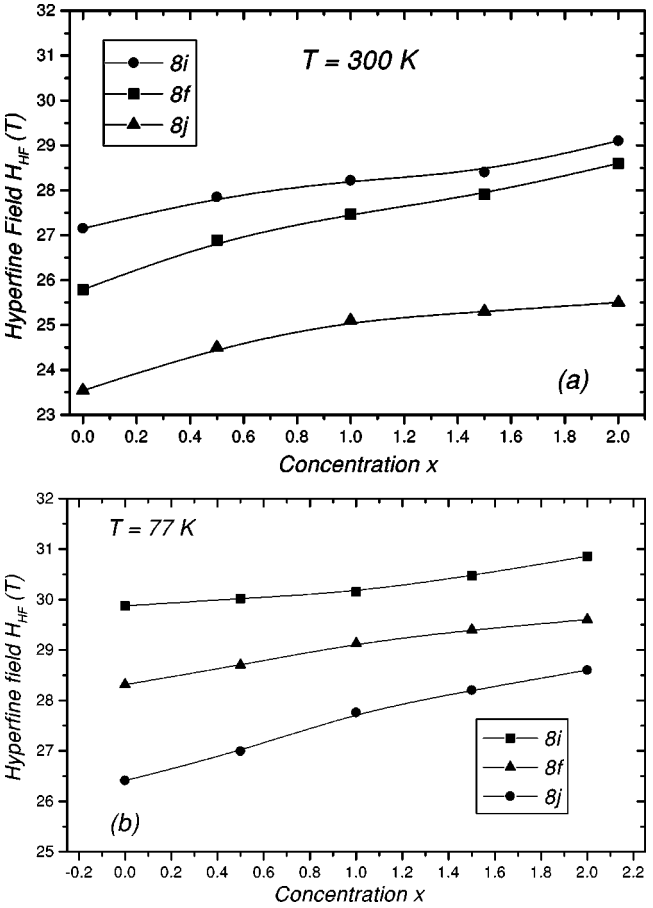

FIG. 14. The compositional dependence of the hyperfine fields for tetragonal phase (a) at 300 K, (b) at 77 K.

field, which is the Fermi contact term, contains contributions from all *s* core electrons and 4*s* valence electrons as proposed above for our analysis and verified here *a posteriori*.

The Mössbauer spectra (Fig. 15) relative to the hexagonal phase are broadened compared with those of the tetragonal phase, where Ti is located on one crystallographic position. According to the structure relationship described in Sec. III, it should be statistically distributed over sites $2e$ and $6l$. Co, located on the $3f$ site in the 1:12 structure, should occupy the $3g$ site. With the highest near Fe neighbors, the $2e$ site, relative to the dumbbells, shows the highest WSC volume. It is obvious from Fig. 1 and through Forker *et al.*[28] that WSC $\{3g\}$ is larger than WSC $\{6l\}$. We have, in a first step, reproduced the experimental spectra with seven broadened sextets with respective abundances equal to crystallographic iron occupancies with the sequence $\delta_i > \delta_j > \delta_f$. A detailed study of the hyperfine parameters in this complex structure is

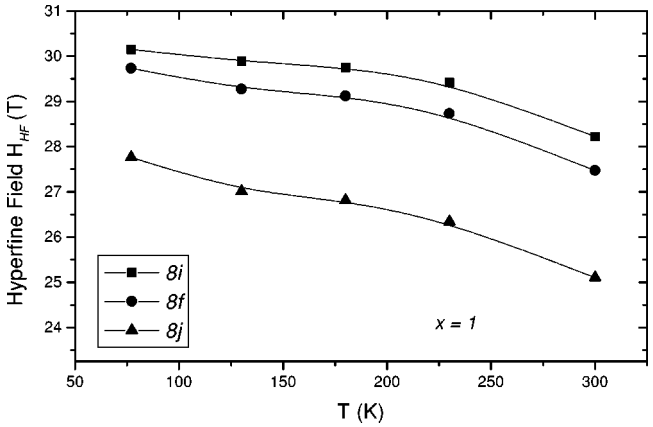

FIG. 13. The temperature dependence of the hyperfine fields in tetragonal $SmFe_{10}CoTi$.

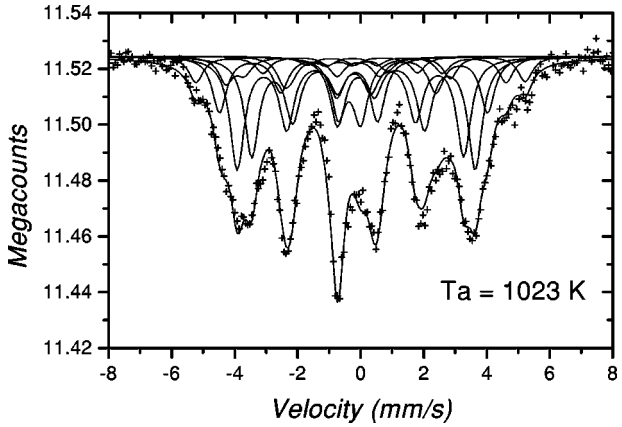

FIG. 15. The 300 K Mössbauer spectrum of hexagonal $SmFe_{10}CoTi$ annealed at 1023 K.

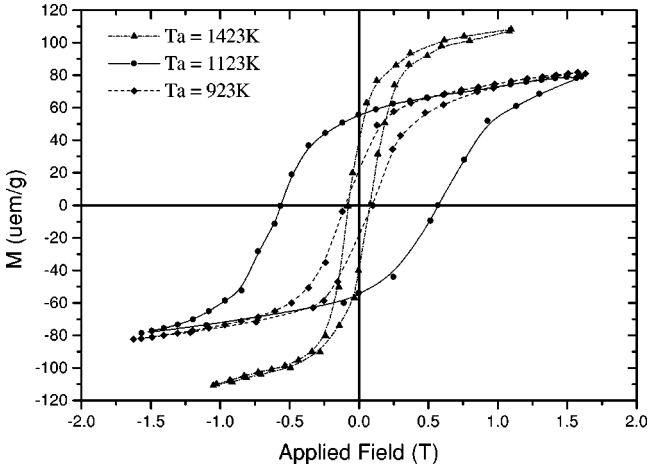

FIG. 16. Hysteresis loops of $SmFe_{9.5}Co_{1.5}Ti$ annealed at indicated temperatures.

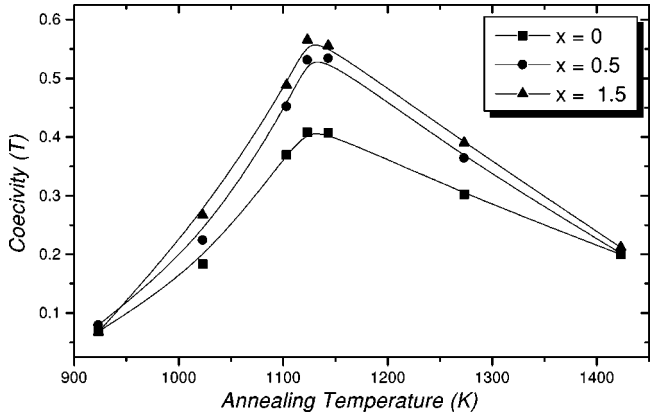

FIG. 17. Coercitive field, at room temperature, versus annealing temperature in $Sm(Fe_{1-x}Co_x)_{11}Ti$ for indicated x values.

in progress. Nevertheless, the mean hyperfine field increases monotonically.

The mean hyperfine field increases in both structures (Fig. 6). This behavior can be correlated directly to the mean magnetic moment variation explained on the basis of a rigid band model.[29] The increase in $3d$-electron number brought by Co fills up asymmetrically the $3d$ subbands.

The nuclear hyperfine fields H_{HF} is the sum of three contributions:

$$H_{HF}=H_{FC}+H_{dip}+H_{orb}.$$

The dipolar field H_{dip} can be neglected because it is small in metals. H_{orb} is produced by the unquenched orbital angular momentum of valence electrons. H_{orb} is positive, is around[30] 2 T, and is assumed constant for all compounds. The Fermi contact term H_{FC} can be divided into two contributions: H_{CE}, the core-electron $(1s,2s,3s)$ polarization field, which is negative, and H_{4s}, the $4s$ conduction-electron polarization field, produced by the Fe $3d$ moment, which is always positive.

By comparing the experimental mean hyperfine field behavior of the $ThMn_{12}$ and $CaCu_5$ structures (Fig. 6), two observations can be made: (i) $|H_{HF}|\{1:12\}$ is greater than $|H_{HF}|\{1:5\}$. This can be explained by the fact that the number of Fe atoms in the 1:12 cell is larger than that in the 1:5 cell. It results in $|H_{CE}|\{1:12\}$ being higher than $|H_{CE}|\{1:5\}$. (ii) The overall mean hyperfine field H_{HF} is negative but the additional $3d$ Co electrons affect the positive H_{4s} term, and its contribution is higher for a 1:5 cell than for a 1:12 cell. Qualitatively, it means that H_{HF} will be reduced faster for the 1:5 compounds than for the 1:12 compounds. This results in a slope, versus Co content, for $H_{HF}\{1:5\}$ to be half of that for $H_{HF}\{1:12\}$.

The hysteresis loops of $SmFe_{9.5}TiCo_{1.5}$ measured at room temperature are illustrated in Fig. 16. The effect of annealing temperature on magnetic properties is demonstrated (see Table IV). The coercive field increases with increasing annealing temperature up to 5.67 kOe (D=35 nm). The small coercivity for an annealing temperature of 920 K must be due to an unfavorable microstructure, probably resulting from a small grain size containing many defects. Furthermore, it is well established that the coercive field H_C decreases with increasing grain size, i.e., with increasing annealing temperature. This is the reason for the small H_C value for samples annealed at $T_A=1423$ K.

Coercivity exhibits two antagonist regimes as a function of T_A (Fig. 17). When increasing T_A, on the one hand, the number of surface defects of the $CaCu_5$ phase are reduced and results in an increase of H_C; on the other hand, the x-ray diffraction domain size of the $ThMn_{12}$ phase increases, which reduces H_C. The intersection of both behaviors occurs around 1123 K where H_C shows a maximum. In this region the two phases $CaCu_5$ (10%) and $ThMn_{12}$ (90%) coexist.

V. CONCLUSIONS

High-energy ball milling and subsequent annealing at $T_A>1173$ K lead to a continuous and homogeneous substitution of Co for Fe in the $I4/mmm$ $SmFe_{11}Ti$ compound. The unit cell parameter a remains constant and c shows a small decrease. The increase of Curie temperature T_C and hyperfine field H_{HF} attest for the Co continuous substitution, corroborated by EDX analysis.

For $T_A<1073$ K a hexagonal $P6/mmm$ $CaCu_5$-type phase, the precursor of the tetragonal $I4/mmm$ $SmFe_{11-x}Co_xTi$ phase, is detected as the main phase. The Rietveld analysis gives a phase stoichiometry described as 1:10, with three crystallographic transition-metal sites 2 $(6l)$ atoms, 3 $(3g)$ atoms, $2s$ $(2e)$, and one Sm site $1-s(1a)$.

For $1093<T_A<1173$ K the hexagonal phase is transformed into the tetragonal phase. We suggest that this evolution is favored by a recovery of the stacking fault between the hexagonal phase and the coexisting bcc phase.

The substitution of Co, which contributes to complete the $3d$ subband, reduces the negative interactions and induces the Curie temperature enhancement in both structures. The hyperfine parameters were assigned on the basis of the calculation of WSC volumes. The isomer shift behavior of the $8i$- and $8j$-site Fe atom is attributed to the additional $3d$ electrons brought by $8f$ Co neighbors. In contrast, no change

is observed for the $8f$ isomer shift. The difference for the $8f$-site behavior corroborates the preferential occupation of Co atoms on this site in the 1:12 structure.

The mean hyperfine field enhancement with cobalt content in both structures might be correlated to the compensation of the core-electron polarization field by the $4s$ polarization field produced by the $3d$ moment. The highest H_C value, 0.6 T, occurs around $T_A = 1123$ K (with $T_C = 790$ K) and suggests that such semihard material is a potential candidate for magnetic recording media.

ACKNOWLEDGMENTS

We are grateful to Dr. J. M. Grenèche for the low-temperature Mössbauer measurements and P. Beaunier for EDX experiments. We should like to thank Professor M. Forker and Professor E. Koch for their helpful discussions.

[1] M. Sagawa, S. Fujimara, N. Togawa, H. Yamamoto, and Y. Matsuara, J. Appl. Phys. **55**, 2083 (1984).
[2] F. R. de Boer, Y. K. Huang, D. B. de Mooij, and K. H. J. Buschow, J. Less-Common Met. **135**, 139 (1987).
[3] K. Ohashi, T. Yokoyama, R. Osugi, and Y. Tawara, IEEE Trans. Magn. **MAG-23**, 3101 (1987).
[4] D. B. de Mooij and K. H. J. Buschow, J. Less-Common Met. **136**, 207 (1988).
[5] H. Saito, M. Takahashi, and T. Wakiyama, J. Appl. Phys. **64**, 5965 (1988).
[6] W. Kaiying, H. Jifan, W. Yizhong, H. Boping, and W. Zhenxin, Phys. Status Solidi A **148**, K29 (1995).
[7] K. H. J. Buschow, J. Appl. Phys. **63**, 3130 (1988).
[8] J. Wecker, M. Katter, and L. Schultz, J. Appl. Phys. **69**, 6058 (1991).
[9] J. Ding, P. G. McCormick, and R. Street, J. Alloys Compd. **191**, 197 (1993).
[10] S. F. Cheng, V. K. Sinha, Y. Xu, J. M. Elbicki, E. B. Boltich, W. E. Wallace, S. G. Sankar, and D. E. Laughlin, J. Magn. Magn. Mater. **75**, 330 (1988).
[11] L. Pareti, M. Solzi, and G. Marusi, J. Appl. Phys. **72**, 3009 (1992).
[12] C. Djega-Mariadassou and L. Bessais, J. Magn. Magn. Mater. **210**, 81 (2000).
[13] A. Teresiak, M. Kubis, N. Matteru, M. Wolf, and K. H. Müller, J. Alloys Compd. **1998**, 284 (1998).
[14] D. Givord, J. Laforest, J. Schweizer, and F. Tasset, J. Appl. Phys. **50**, 2008 (1979).
[15] A. Moukarika, V. Papefthymiou, T. Bakas, V. Psycharis, and D. Niarchos, J. Magn. Magn. Mater. **163**, 109 (1996).
[16] H. M. Rietveld, Acta Crystallogr. **22**, 151 (1967).
[17] J. Rodríguez-Carvajal, Physica B **192**, 55 (1993).
[18] P. Thompson, D. E. Cox, and J. B. Hasting, J. Appl. Crystallogr. **20**, 79 (1987).
[19] Q. F. Xiao, Z. D. Zhang, T. Zhao, W. Liu, C. Sui, X. G. Zhao, and D. Y. Geng, J. Appl. Phys. **82**, 6170 (1997).
[20] Z. W. Li, X. Z. Zhou, and A. H. Morrish, J. Appl. Phys. **69**, 5602 (1991).
[21] B. Hu, K. Wang, Y. Wang, Z. Wang, Q. Yan, and X. Sun, Phys. Rev. B **51**, 2905 (1995).
[22] D. Givord and R. Lemaire, IEEE Trans. Magn. **10**, 109 (1974).
[23] O. Mozo, L. Pareti, M. Solzi, and W. J. F. Davis, Solid State Commun. **66**, 465 (1988).
[24] S. M. Pan, H. Chen, Z. X. Xu, R. Z. Ma, J. L. Yang, B. S. Zhang, D. Y. Xue, and Q. Ni, J. Appl. Phys. **76**, 6720 (1994).
[25] Y. C. Yang, H. Song, L. S. Kong, J. L. Yuang, Y. F. Ding, and H. M. Zhou, J. Appl. Phys. **64**, 5968 (1988).
[26] R. Coehoorn, C. M. J. Denissen, and R. Eppenga, J. Appl. Phys. **69**, 6222 (1991).
[27] Gary J. Long, S. Mishra, O. A. Pringle, F. Grandjean, and K. H. J. Buschow, J. Appl. Phys. **75**, 5994 (1994).
[28] M. Forker, A. Julius, M. Schulte, and D. Best, Phys. Rev. B **57**, 11 565 (1998).
[29] A. M. van Diepen and K. H. J. Buschow, J. Appl. Phys. **43**, 645 (1972).
[30] M. B. Stream, in Landolt-Börnstein, New Series, Group III, Vol. 19a, edited by K. H. Hellwege and O. Madelung (Springer, Berlin, 1987).